Journal of the Mechanics and Physics of Solids 57 (2009) 51–66

Contents lists available at ScienceDirect

Journal of the Mechanics and Physics of Solids

journal homepage: www.elsevier.com/locate/jmps

Mixed-mode interfacial adhesive strength of a thin film on an anisotropic substrate

Rajesh Kitey [a], Philippe H. Geubelle [a], Nancy R. Sottos [b,*]

[a] Department of Aerospace Engineering, Beckman Institute for Advanced Science and Technology, University of Illinois at Urbana-Champaign, IL 61801, USA
[b] Department of Materials Science and Engineering, Beckman Institute for Advanced Science and Technology, University of Illinois at Urbana-Champaign, IL 61801, USA

ARTICLE INFO

Article history:
Received 6 May 2008
Received in revised form
30 September 2008
Accepted 7 October 2008

Keywords:
Dynamic wave propagation
Laser spallation
Mixed-mode loading
Thin film
Decompression shock

ABSTRACT

The mixed-mode interfacial adhesion strength between a gold (Au) thin film and an anisotropic passivated silicon (Si) substrate is measured using laser-induced stress wave loading. Test specimens are prepared by bonding a fused silica (FS) prism to the back side of a ⟨100⟩ Si substrate with a thin silicon nitride (Si_xN_y) passivation layer deposited on the top surface. A high-amplitude stress wave is developed by pulsed laser ablation of a sacrificial absorbing layer on one of the lateral surfaces of the FS prism. Due to the negative non-linear elastic properties of the FS, the compressive stress wave evolves into a decompression shock with fast fall time. Careful selection of the incident angle between the pulse and the FS/Si interface generates a mode-converted shear wave in refraction, subjecting the Si_xN_y/Au thin film interface to dynamic mixed-mode loading, sufficient to cause interfacial fracture. A detailed analysis of the anisotropic wave propagation combined with interferometric measurements of surface displacements enables calculation of the interfacial stresses developed under mixed-mode loading. The mixed-mode interfacial strength is compared to the interfacial strength measured under purely tensile loading.

1. Introduction

Multilayer thin film devices have widespread engineering applications from microelectronics to pharmaceutical industries. In most engineering applications, interfacial failure and the subsequent film delamination remain a major reliability concern as interfacial properties, in particular interfacial adhesion and interfacial fracture toughness, govern the mechanical integrity of thin film devices. Significant effort has been devoted to the development of test procedures for the measurement of thin film adhesion, including the peel, pull, blister, and indentation test methods (Mittal, 1976). During all these tests, the interface is subjected to high stress levels and consequent inhomogeneous deformations (Kim and Kim, 1988; Yu et al., 2001). Large amounts of plastic deformation can result (especially in the peel test) and dominate the behavior during the test (Thouless, 1994). Although these tests are simple to perform and useful for basic adhesion characterization, the stress fields are difficult to analyze and separate from the measured adhesion energy. Characterization of ductile or strongly adhered films is also difficult or in some cases impossible by these methods (Kim and Kim, 1988; Kriese et al., 1999a, b). The resulting adhesion measurements tend to be qualitative and provide a more comparative assessment.

* Corresponding author.
E-mail address: n-sottos@uiuc.edu (N.R. Sottos).

0022-5096/$ - see front matter © 2008 Elsevier Ltd. All rights reserved.
doi:10.1016/j.jmps.2008.10.002

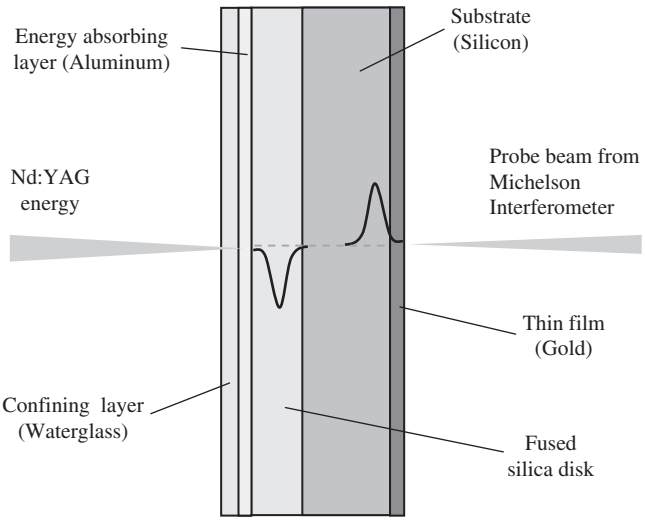

Fig. 1. Schematic of tensile laser spallation specimen geometry.

In contrast to the adhesion tests described above, laser spallation techniques (Yang, 1974; Vossen, 1978; Gupta et al., 1990; Wang et al., 2002) involve dynamic loading of a thin film interface in a precise, non-contacting manner with laser-generated stress waves. The high-amplitude, short-duration stress wave is developed by pulsed laser ablation of a sacrificial absorbing layer on the back surface of a substrate as shown schematically in Fig. 1. A compressive longitudinal stress wave, with a shape similar to that of the laser pulse, is emitted from the absorbing layer and propagates towards a thin film deposited on the front surface of the substrate. The reflected tensile wave from the film's free surface loads the film/substrate interface in tension. The laser energy is increased until a longitudinal wave is generated with amplitude sufficient to generate interfacial failure. From interferometric displacement measurements at the free surface, the stress history at the interface is inferred using standard wave mechanics and the maximum stress acting on the interface is calculated. If a non-linear substrate such as fused silica (FS) is used, the compressive stress pulse will evolve into a decompression shock due to the non-linear strain softening characteristic of the substrate (Gupta et al., 2003; Wang et al., 2002, 2003). The rapid fall time of the shock significantly enhances loading of the interface.

In most adhesion tests, the loading is predominately of tensile (mode I) nature, while, in most commercial applications, thin films tend to fail under mixed-mode conditions (Evans and Hutchinson, 1995). The presence of multiple thin film layers and large mismatch of properties across interfaces greatly complicates the characterization of mixed-mode performance. Several fracture-based techniques have been proposed for investigating mixed-mode failure of thin film interfaces including flexure (Cao and Evans, 1989; Charalambides et al. 1990), double cantilever beam (Thouless, 1989, 1994), and Brazil-nut specimen (Wang and Suo, 1990) test methods. All of these techniques require the thin film interface of interest to be sandwiched between two elastic substrates via a bonding process. A pre-crack is introduced into the bonded stack and the strain-energy release rate is measured by propagating the crack. These methods are limited by the intricate sample preparation and the bonding process, which can cause undesirable compositional changes in many films. Moreover, in some thin film systems, it is difficult to introduce a pre-crack and grow the crack in a controlled manner along the interface of interest (Hartfield et al., 2004).

Recently, Wang et al. (2004) and Hu and Wang (2006) successfully modified the laser spallation technique to achieve dynamic mixed-mode loading of thin film interface without a sandwich configuration. By allowing the stress pulse to mode convert as it reflects from an oblique surface of a FS triangular prism, a high-amplitude shear wave was generated and used to delaminate a thin film deposited directly on the opposite surface of the prism. By changing the geometry of the prism, Hu and Wang (2006) were able to achieve nearly pure mode II loading of a thin film interface. Here we expand on this novel method to characterize the mixed-mode interface strength of a thin film deposited on a passivated Si substrate.

In the current investigation, a FS prism is bonded directly to the back surface of a passivated Si substrate with a gold (Au) thin film deposited on the opposite surface. The FS enables generation of a high-amplitude decompression shock with a rapid fall time. Careful selection of the incident angle between the pulse and the FS/Si interface generates a mode-converted shear wave in refraction subjecting the Au thin film interface to dynamic mixed-mode loading sufficient to cause interfacial fracture. In contrast to an isotropic material like FS, the wave angles and wave speeds are interdependent in the anisotropic Si substrate. Through analysis of the anisotropic wave propagation, we are able to infer the mixed-mode interfacial strength of the Au film as deposited on the passivated Si substrate.

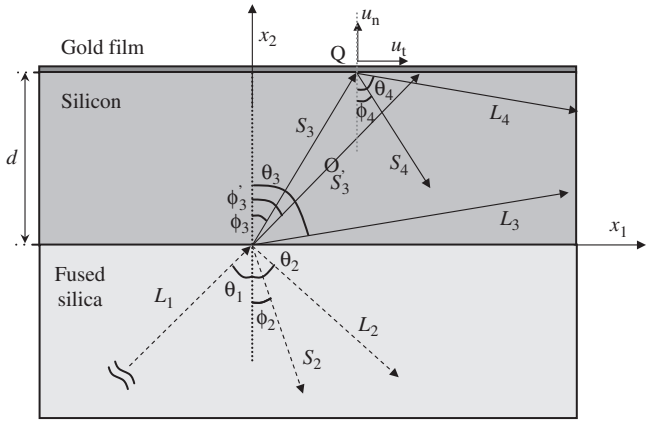

Fig. 2. Wave propagation across an isotropic–cubic bimaterial interface in x_1–x_2 plane. The bimaterial interface lies in the x_1–x_3 plane. A longitudinal wave L_1 is incident at an angle θ_1 from the normal to the interface x_2 in x_1–x_2 plane. Mode conversion at the interface yields two reflected waves, L_2 (longitudinal) and S_2 (shear) in the fused silica and three refracted waves, L_3 (quasi-longitudinal), S_3 (quasi-shear), and S_3' (pure shear) in the anisotropic (cubic) silicon layer. The reflected and refracted waves propagate with angles θ_2, ϕ_2, θ_3, ϕ_3, and ϕ_3', respectively, from the normal to the interface. S_3 further mode converts into longitudinal wave L_4 and shear wave S_4 at the Si/Au film interface.

Table 1
Relevant material properties

Material	Density (kg/m^3)	Longitudinal wave speed (m/s)	Shear wave speed (m/s)
Fused Silica (FS)[a]	2200	6000	3772
Silicon (Si)[b,c]	2329	8387	4563
Gold (Au)[d]	19282	3275	1475

[a] Fukuhara and Sanpei (1994).
[b] Wave speeds are in (1,0,0) direction.
[c] Hall (1967).
[d] Neighbours and Alers (1958).

2. Analysis of wave propagation in anisotropic media

An analytical study of wave propagation across the FS/Si interface is conducted to determine the optimum specimen configuration and extract the mixed-mode interfacial strength from out-of-plane interferometric measurements. As shown in Fig. 2, the coordinate axes are chosen such that the planes of material symmetry (cubic $\langle 1\,0\,0\rangle$ Si planes) coincide with coordinate planes. The x_1–x_3 plane is coincident with the isotropic FS/cubic Si bimaterial interface and the wave propagation is constrained in the x_1–x_2 plane. The longitudinal wave L_1, generated in FS, impinges the interface at an angle θ_1 and mode converts back into the FS as longitudinal and shear waves, L_2 and S_2, respectively. The incident wave also generates three refracted waves in the Si (Nayfeh, 1995), L_3 (quasi-longitudinal wave), S_3 (quasi-shear wave), and S_3' (pure shear wave). The wave velocities are related to their respective wave angles from the interface normal x_2 by Snell's law:

$$\frac{v_{L_1}}{\sin\theta_1}=\frac{v_{L_2}}{\sin\theta_2}=\frac{v_{S_2}}{\sin\phi_2}=\frac{v_{L_3}}{\sin\theta_3}=\frac{v_{S_3}}{\sin\phi_3}=\frac{v_{S_3'}}{\sin\phi_3'}. \tag{1}$$

For a given angle of incidence θ_1, the reflected longitudinal and shear wave angles, θ_2 and ϕ_2, respectively, are determined by the longitudinal and shear wave velocities in FS (Table 1). The calculation of the refracted wave angles in Si (θ_3, ϕ_3, and ϕ_3'), however, is not straightforward since the wave velocities depend upon the direction of wave propagation. Eq. (1) is solved numerically for refracted longitudinal and shear wave speeds and their corresponding wave angles by substituting wave speeds from Eq. (A.4), described in Appendix A. The cubic Si material constants (elements of stiffness matrix), $C_{11}=1.639\times10^{11}$, $C_{12}=0.648\times10^{11}$, and $C_{44}=0.792\times10^{11}$ N/m^2 (Hall, 1967), are used in the calculations.

2.1. Wave speed and wave angles at the FS/Si interface

Fig. 3(a) shows the variation of wave angles with the angle of incidence, θ_1. The solid and dashed curves correspond to the refracted wave angles in Si and the reflected wave angles in FS, respectively. Wave angles increase monotonically with

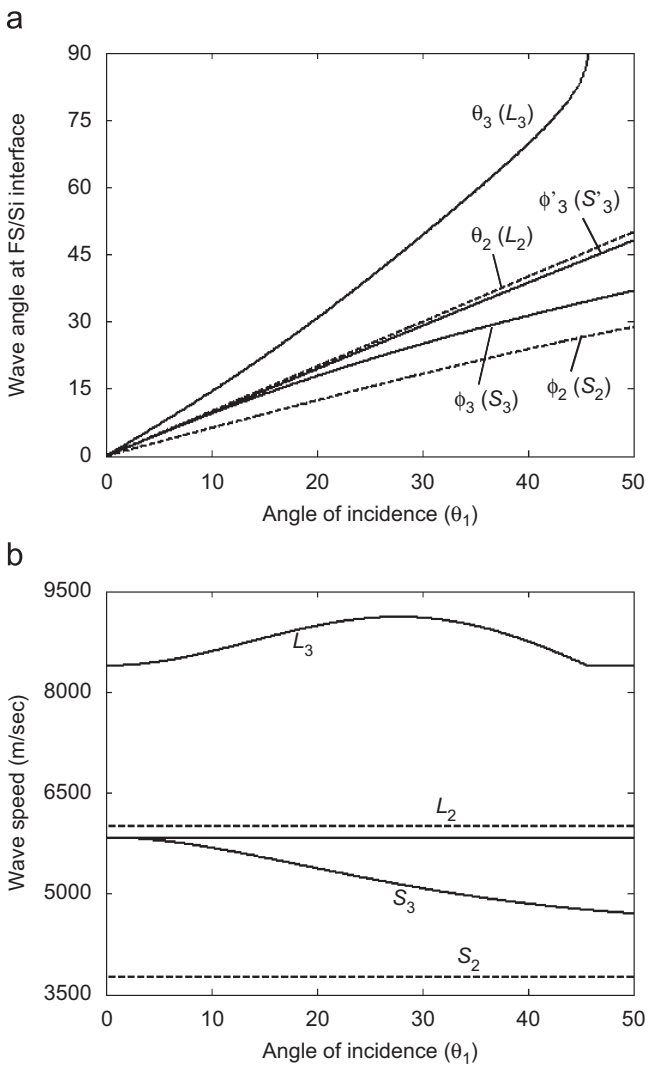

Fig. 3. Variation of (a) wave angles and (b) wave speeds at the FS/Si interface with varying angle of incidence (of longitudinal wave) in FS.

θ_1, and the longitudinal and shear wave angles in Si are larger than the respective angles in FS. The longitudinal wave angles both in FS and in Si are larger compared to their shear counterparts. For the angle $\theta_1 = 45.7^\circ$ (defined as a critical angle θ_{1c}), L_3 propagates along the interface and becomes evanescent (Nayfeh, 1995). The incidence angles greater than θ_{1c} are not considered for designing the specimen geometry. In Fig. 3(b), the wave speeds of both L_3 and S_3 (slow shear wave) vary with the angle of incidence, whereas S_3' (fast shear wave) has a constant wave speed of 5831 m/s irrespective of its propagation direction. The wave speeds are not plotted explicitly with their respective wave angles but the two can be correlated by comparing Figs. 3(a) and (b). The wave speed of L_3 varies between 8390 m/s (at $\theta_3 = 0^\circ$) and 9116 m/s (at $\theta_3 = 45^\circ$), whereas the limiting wave speeds for S_3 are 5831 and 4614 m/s, at $\phi_3 = 0^\circ$ and 67° (not shown), respectively. The reflected waves L_2 and S_2, travel in FS with constant speeds 6000 and 3772 m/s, respectively.

2.2. Polarization vectors and amplitude ratios at the FS/Si interface

The direction of particle motion (polarization vector) determines the component of the wave amplitude contributing to the in-plane and out-of-plane displacement components at the film surface. The polarization vector of a wave component, p_v, is calculated by solving the Cristoffel equation as described in Appendix A (Eq. (A.2)). In an anisotropic material, the polarization vector is usually skewed and its degree of skewness depends upon the wave propagation direction in contrast to an isotropic material where it is parallel/perpendicular to the direction of longitudinal/shear wave propagation (e.g. $(\sin\theta_2, -\cos\theta_2, 0)$ and $(\cos\phi_2, \sin\phi_2, 0)$ for L_2 and S_2, respectively, in the current investigation). As shown in Fig. 4(a), the

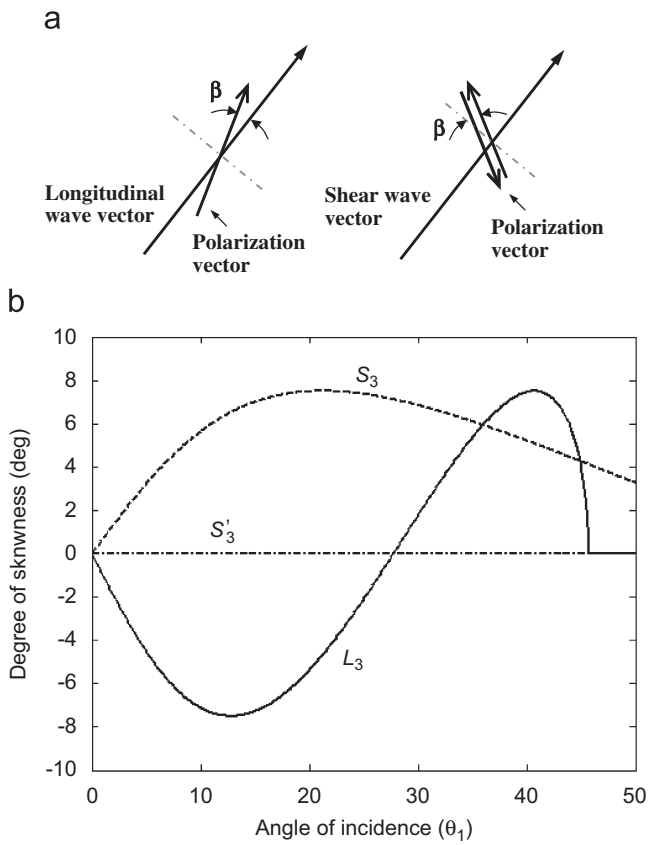

Fig. 4. (a) Degree of skewness, β, in longitudinal and shear waves and (b) variation of β in Si for increasing angle of longitudinal wave incidence, θ_1, at the FS/Si interface.

degree of skewness, β, is defined as the angle between a longitudinal wave vector and the direction of particle motion. In the case of a shear wave, β is the angle between in-plane normal to the shear wave direction and the particle motion vector. The value of β for refracted waves L_3, S_3, and S_3' in silicon is shown in Fig. 4(b) as a function of the angle of incidence θ_1. The waves L_3 and S_3 are called quasi-longitudinal and quasi-shear waves, respectively, due to their non-zero β. The maximum magnitude of skewness is $\sim 7.5^\circ$ for both waves. The S_3' has zero skewness for all incident angles, which implies that S_3' remains a pure shear wave for all propagation directions. The L_3 wave attains zero skewness at $\theta_3 = 45^\circ$, which also corresponds to $\theta_1 = 27.75^\circ$. At this wave angle, L_3 attains the maximum wave speed. Beyond θ_{1c}, L_3 propagates as a pure longitudinal wave along the interface. In contrast, the quasi-shear wave S_3 propagates with zero skewness at $\phi_3 = 45^\circ$ when its wave speed is minimum (or at $\theta_1 = 66.85^\circ$, not shown in plots). In FS, both the reflected waves, L_2 and S_2, have zero degree of skewness and propagate as pure longitudinal and shear waves.

For an incident longitudinal wave at the Si/FS interface, the amplitude ratio of scattered waves is calculated as described in Appendix A (Eq. (A.8)). The amplitude ratio variation of the reflected and refracted waves with increasing angle of incidence is presented in Fig. 5. As the critical angle of incidence is approached, the variation in amplitude ratio for the longitudinal waves is more dramatic than for their shear wave counterparts. The zero amplitude ratio for the pure shear wave (S_3') indicates that no component of the incident energy is transferred to S_3'.

2.3. Wave parameters at the Si/Au interface

The quasi-shear wave S_3, oblique to the Si/Au interface, is mode converted into another quasi-shear wave S_4, a pure shear wave S_4' (not shown due to its zero amplitude ratio, similar to the case of S_3') and a quasi-longitudinal wave L_4 (Fig. 2). To interpret experimental measurements of out-of-plane displacement at the point-of-interest, Q, we correlate in-plane and out-of-plane displacement components to the incident and reflected wave parameters. The variation in wave angles and wave speeds of S_4 and L_4 with the incident angle θ_1 is similar to the plots for S_3 and L_3, in Fig. 3. The degree of skewness is determined by reversing the signs of S_3 and L_3 in Fig. 4(b). The amplitude ratios of S_4 and L_4, A_{S_4}/A_{S_3}, and A_{L_4}/A_{S_3}, respectively, are evaluated by solving traction continuity equations tangential and normal to the free surface as described

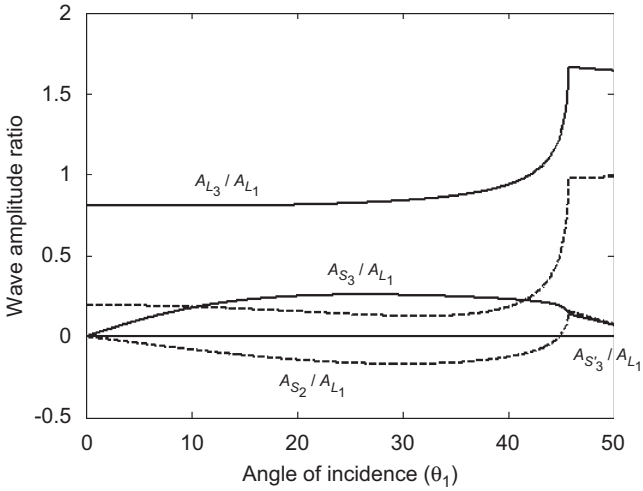

Fig. 5. Amplitude ratios of reflected and refracted longitudinal/shear waves at the FS/Si interface for varying angle of incidence of longitudinal wave.

in Appendix (Eq. (A.9)) and plotted in Fig. 6(a) as a function of the angle of incidence θ_1. For an incident wave normal to the interface ($\theta_1 = 0$), the amplitude ratios for the reflected longitudinal and shear waves are 0 and 1, respectively. The amplitude ratio of the longitudinal wave L_4 increases with increasing θ_1. The variation is more rapid as the critical angle is approached. On the other hand, the amplitude ratio of shear wave decreases with increasing θ_1 until before reaching the critical angle. The free surface displacement at Q is determined by applying displacement continuity parallel and perpendicular to the interface:

$$u_t = p_1^{S_3}A_{S_3} + p_1^{S_4}A_{S_4} + p_1^{L_4}A_{L_4} = \left(p_1^{S_3} + p_1^{S_4}\frac{A_{S_4}}{A_{S_3}} + p_1^{L_4}\frac{A_{L_4}}{A_{S_3}}\right)A_{S_3},$$
$$u_n = p_2^{S_3}A_{S_3} + p_2^{S_4}A_{S_4} + p_2^{L_4}A_{L_4} = \left(p_2^{S_3} + p_2^{S_4}\frac{A_{S_4}}{A_{S_3}} + p_2^{L_4}\frac{A_{L_4}}{A_{S_3}}\right)A_{S_3}. \quad (2)$$

The ratio of in-plane to the out-of-plane displacement u_t/u_n is shown in Fig. 6(b). For small angle of incidence, θ_1, the displacement ratio is large, suggesting that the loading is predominately shear. The displacement ratio also rises dramatically as the critical angle of incidence is approached, which again suggests that the shear mode dominates. Hence, an angle of incidence close to the critical angle maximizes the shear component of the mixed-mode loading.

3. Experimental procedure

3.1. Specimen geometry

Our specimen design is based on the analytical study of wave propagation across the FS/Si interface described in Section 2, as well as the previous experiments performed by Wang et al. (2004). We can measure the out-of-plane displacement history at point Q (Fig. 2) if the spatial distance in between the arrival of L_3 and S_3 at the free surface is larger than the diameter of the probe beam. Since the spatial separation between waves increases as the angle of incidence increases, a 45° right-angled FS prism (of dimension 10 mm × 10 mm × 10 mm) is chosen to prepare the specimen and provide an angle of incidence just below the critical angle ($\theta_{1c} = 45.7°$).

The thin film samples consisted of an Au film deposited by E-Beam evaporation onto a 730 μm thick Si (⟨1 0 0⟩) substrate with a 400 nm Si_xN_y passivation layer. The passivation layer on top of the Si serves as a dielectric barrier. In microelectronic devices this layer also protects the underlying integrated circuit structure from moisture and contamination. Kandula et al. (2008) have shown that a thin Si_xN_y layer does not influence the wave propagation, and in turn the state of stress at the film interface. They have also found that the substrate surface roughness significantly affects the thin film interfacial strength.

In the current work, the surface roughness of the Si_xN_y layer was 32 nm, as measured by atomic force microscopy (AFM). Three different Au film thicknesses, 300, 600, and 1200 nm, were examined. The FS prism was prepared by depositing a 400 nm layer of aluminum (Al) on one of the perpendicular lateral surfaces using E-beam evaporation, followed by spin-coating of 10 μm waterglass confining layer on top of the Al layer. The waterglass thickness was controlled by varying the

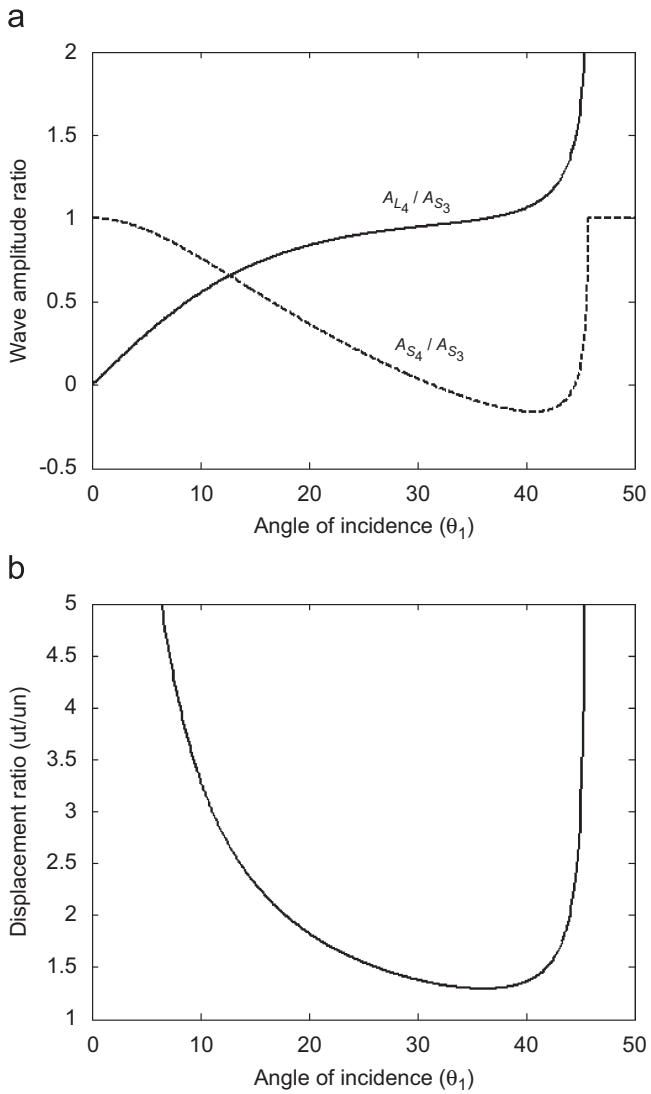

Fig. 6. Variation of amplitude ratio and the displacement ratio at substrate/film interface with the increasing angle of incidence. (a) Amplitude ratios of reflected longitudinal and shear waves at Si/Au interface with respect to an incident shear wave L_1 at FS/Si interface. (b) The ratio of in-plane to the out-of-plane displacement at the Si/Au interface.

spin speed and solution concentration. The waterglass layer assists in developing a laser-induced high-amplitude compressive stress pulse in the substrate by constraining the energy absorbing layer. The back surface of the Au thin film/Si substrate specimen was then bonded to the FS prism base by applying a thin UV-bond at the FS/Si interface (Fig. 7(a)). While bonding, the prism edges were carefully aligned parallel to the $\langle 1\,0\,0 \rangle$ Si planes. The adhesive UV-bond layer was then cured by exposing the bonded interface to UV radiation for about an hour.

Additional experiments were conducted to evaluate the intrinsic tensile adhesion strength of the Au film onto the Si_xN_y passivated Si substrate. In this case, the Au film/Si substrate specimen was bonded to a 500 μm thick FS plate instead of a prism. The specimen geometry was similar to as shown in Fig. 1. A 400 nm Al layer was deposited on the back of the FS, followed by spin coating of a 1 μm waterglass constraining layer. The thinner waterglass layer was applied to decrease the stress amplitude.

3.2. Experimental setup

The mixed-mode experimental setup is shown schematically in Fig. 7(b). The specimen was aligned in a Michelson interferometer such that an argon-ion beam ($\lambda = 514\,\text{nm}$) was focused perpendicular to the film surface

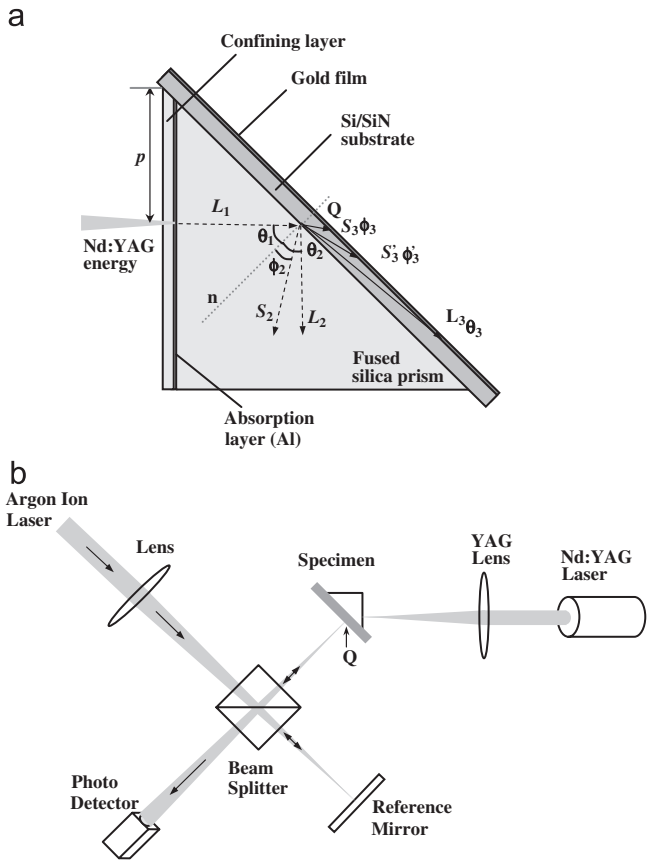

Fig. 7. (a) Schematic of the FS–Si/Si_xN_y/Au bonded specimen configuration and (b) Michelson interferometric setup for the measurement of free surface displacements.

(to the smallest possible focal spot ($\sim$100 μm)) at the point-of-interest *Q*. The 1.2 mm diameter YAG beam was focused on the Al/waterglass layer deposited on the adjacent lateral surface to the FS prism base. Care was taken to maintain the incident YAG beam in-plane with one of the Si planes of material symmetry. An 8 ns duration Gaussian pulse of variable energy content from the Nd:YAG laser ($\lambda = 1064$ nm) impinged on the Al layer, developing a high-amplitude compressive stress pulse in the FS, which propagated towards the bonded Si substrate at an angle determined by the prism angle (45° in current specimen configuration). Due to the non-linear elastic properties of FS in compression, the initial Gaussian stress pulse evolved into a sharp stress pulse (which eventually generated a weak decompression shock) as it traveled into the FS (Gupta et al., 2003; Wang et al., 2003). The incident stress pulse oblique to the FS/Si interface was mode converted into reflected and refracted longitudinal and shear waves (see Fig. 7(a)). The refracted shear wave, S_3, loaded the film in mixed-mode at the passivated Si/Au interface.

3.3. Fringe analysis

Using the analysis in Section 2, the substrate stress and interface stress histories are inferred from the displacement fringe data recorded at point *Q*. The mode-converted wave parameters corresponding to the 45° angle of incidence are summarized in Table 2. The fringe order *N* of the interferogram is related to out-of-plane displacement, u_n, and the wave length of the probe beam, λ, by

$$u_n(t) = \frac{\lambda}{2} N(t). \tag{3}$$

The fringe order $N(t)$ at a given time instant t is obtained from

$$I(t) = \frac{I_{\max} + I_{\min}}{2} + \frac{I_{\max} - I_{\min}}{2} \sin 2\pi N(t), \tag{4}$$

Table 2
Mode converted wave parameters for the angle of incidence $\theta_1 = 45^\circ$

Wave (w)	Wave angle from interface normal	Wave speed (m/s)	Polarization vector	Amplitude ratio[a] with incident wave (A_w)
L_2	45.0° (θ_2)	6000	(0.71, −0.71, 0)	0.527
S_2	26.5° (ϕ_2)	3772	(0.90, 0.45, 0)	0.012
L_3	83.8° (θ_3)	8436	(0.98, 0.18, 0)	1.258
S_3	34.2° (ϕ_3)	4765	(−0.78, 0.62, 0)	0.187
S_3'	43.4° (ϕ_3')	5831	(0, 0, 1)	0
L_4	83.8° (θ_4)	8436	(0.98, −0.18, 0)	1.658
S_4	34.2° (ϕ_4)	4765	(−0.78, −0.62, 0)	0.116

[a] Amplitude ratios for waves L_2, S_2, L_3, S_3, and S_3' are with respect to the amplitude of the incident wave L_1, whereas for L_4 and S_4 the magnitudes are with respect to the amplitudes of the quasi-shear wave S_3.

where I_{max} and I_{min} are the maximum and minimum fringe intensities, respectively. Substituting polarization vectors and amplitude ratios from Table 2 into Eq. (2) yields

$$u_t = 0.757 A_{S_3},$$
$$u_n = 0.255 A_{S_3}. \tag{5}$$

From Eq. (5) and Fig. 6, the ratio of in-plane to the out-of-plane displacement for $\theta = 45^\circ$ is

$$u_t/u_n = 2.972. \tag{6}$$

For a shear wave incident oblique to the substrate/film interface, the substrate stress associated to shear wave S_3, τ_{sub}, and the normal and tangential interface stresses, σ_{int} and τ_{int}, respectively, are calculated by substituting Eqs. (5) and (6) into the expressions previously derived by Wang et al. (2004) as

$$\tau_{sub} = -\frac{1}{2}\rho_{sub} C^s_{sub} \frac{\partial A_{S_3}}{\partial t} = -\frac{1}{2 \times 0.255}\rho_{sub} C^s_{sub} \frac{\partial u_n}{\partial t}, \tag{7}$$

$$\sigma_{int} = \rho_{film} h_{film} \frac{\partial^2 u_n}{\partial t^2}, \tag{8}$$

$$\tau_{int} = \rho_{film} h_{film} \frac{\partial^2 u_t}{\partial t^2} = 2.972 \rho_{film} h_{film} \frac{\partial^2 u_n}{\partial t^2}, \tag{9}$$

where ρ_{sub} and ρ_{film} are the density of the substrate and the film, respectively, and h_{film} is the film thickness. The shear wave speed in the substrate, C^s_{sub}, corresponds to the refracted shear wave S_3, traveling at an angle ϕ_3.

4. Results

4.1. Observations of interfacial failure

Mixed-mode film failure is achieved at varying laser fluence for different offset distances. The offset distance, p, as shown in Fig. 7(a) is the distance of the incident YAG energy spot from the FS prism edge. Representative images of film damage due to mixed-mode loading are shown in Figs. 8–10. As observed previously by Wang et al. (2004), the wrinkles and tear damage indicate the presence of mode mixity in the interfacial failure. The effect of laser fluence on the failure of the 600 nm Au film is shown in Figs. 8(a) and (b). For a constant 1.3 mm offset distance, the interfacial damage increases with the increasing incident laser fluence. For the case of lower incident energy (27 mJ/mm^2), relatively small but distinctly spaced wrinkles initiate in the film. The converging direction of wrinkles indicates the direction of shear stress on the film side of the interface (from left to right in the micrographs). More significant wrinkling and tearing occur when the incident energy is doubled (see Fig. 8(b)). Further increase in laser fluence to 67 mJ/mm^2 produces two distinct spallation marks similar to the ones shown in Fig. 10(a) for the 1200 nm film specimen.

Figs. 9 and 10 summarize the effect of offset on the interfacial failure in 1200 nm thick film specimen for the incident energy pulse of 132 mJ/mm^2. For a 2.4 mm offset distance, the film failure takes a horseshoe shape, perhaps due to the convergence of two wrinkles at higher laser power (Fig. 9(a)). The different film spallation pattern observed at $p = 4.7$ mm in Fig. 9(b) is attributed to increased stress attenuation for larger wave travel distance. The failure behavior is more dramatic when the YAG energy is impinged at smaller offsets. For $p = 0.8$ mm, two different spallation spots, Q_1 and Q_2, are generated 1.1 mm apart as shown in Fig. 10(a). At Q_1, the film is completely spalled with several tear marks. At Q_2,

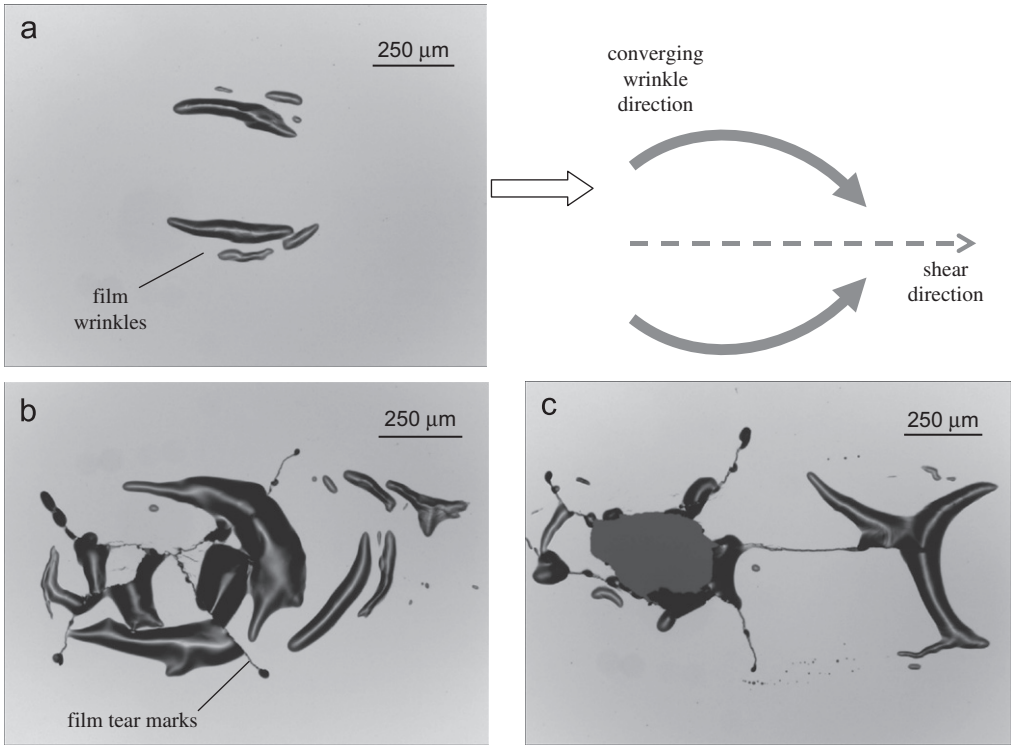

Fig. 8. Effect of laser fluence (Γ) on the failure of a 600 nm thick Au film deposited on a passivated Si substrate. The interfaces are subjected to laser-induced transient mixed-mode loading at an offset, $p = 1.3$ mm, and laser fluence (a) $\Gamma = 20$ mJ/mm^2, (b) $\Gamma = 39$ mJ/mm^2, and (c) $\Gamma = 67$ mJ/mm^2. Schematic associated with (a) shows the directions of converging wrinkles and the direction of applied shear during mixed-mode loading.

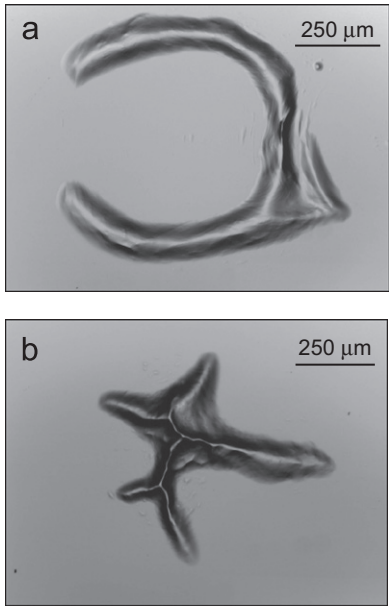

Fig. 9. Effect of offset distance, p, on the failure of a 1200 nm thick Au film deposited on a passivated Si substrate: The laser fluence is 97 mJ/mm^2 and the offsets (a) $p = 2.4$ mm and (b) $p = 4.7$ mm.

significant wrinkle damage is evident. The second spallation spot is not caused by the other refracted wave, since L_3 is spatially separated from Q_1 by approximately 6 mm. Rather, multiple reflections of S_2 in the Si substrate generate the two spallation spots, as depicted in Fig. 10(b). At small offset p, the reflected wave has enough energy to fail the Si/Au interface at Q_2, in addition to the interfacial failure due to the first incident wave at Q_1. Interestingly, the converging direction of wrinkles in Fig. 10(a) is opposite to the wrinkle direction evident in Fig. 8. The reversed direction of the shear failure is

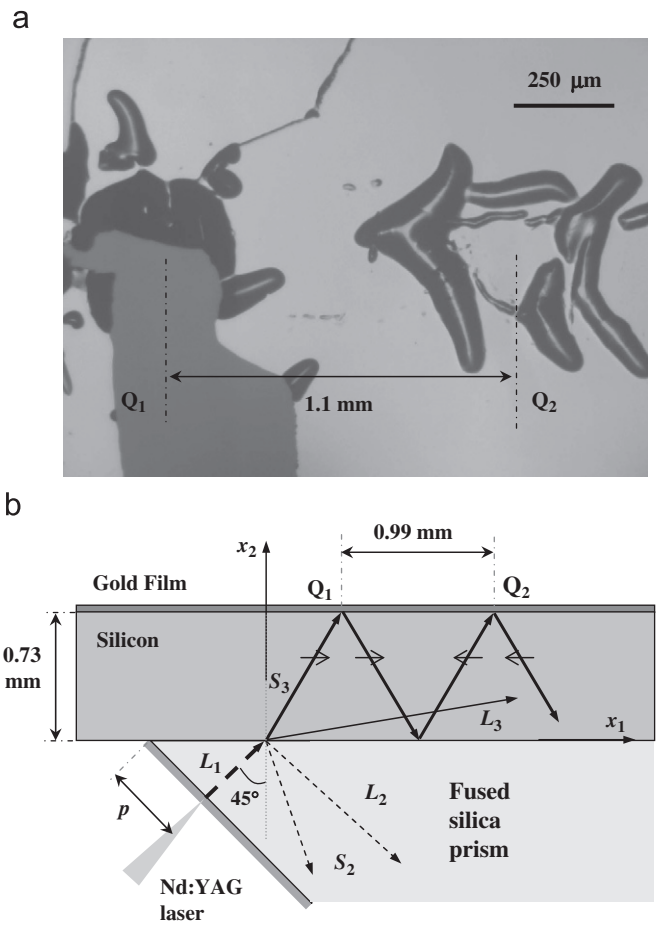

Fig. 10. (a) Multiple spallation spots (Q_1 and Q_2) in a 1200 nm film specimen for an incident energy pulse of 97 mJ/mm^2 at an offset $p = 0.8$ mm. Two spallation marks are developed due to the multiple reflections of shear wave, S_3, as shown in the schematic (b).

another indication that the failure has occurred due to the reflected shear wave. Our analysis predicts that the Q_1 and Q_2 are spatially separated by 0.99 mm, which is close to the observed center-to-center distance between two spallation spots (1.1 mm).

4.2. Quantitative analysis of interface strength

4.2.1. Interferometric data

Representative interferometric measurements are shown in Fig. 11 for a 600 nm film specimen tested at a fluence of 27 mJ/mm^2 and offset distance of 1.3 mm. The shear wave arrival time is 473 ns, which agrees well with analytical calculations. At 508 ns, a sharp turning point (denoted by a solid arrow) indicates the arrival of the decompression shock. The presence of the turning point also verifies the transmission of the decompression shock, generated in the FS, across the FS/Si interface. Fig. 11(b) shows the out-of-plane displacement history, $u_n(t)$, calculated from the interferometric fringe data (Fig. 11(a)) using Eq. (3). The displacement increases monotonically until the turning point. The shear wave S_3, incident oblique to the interface, generates both in-plane and out-of-plane displacements, which are related to each other by Eq. (6) for the current specimen geometry. Wang et al. (2004) previously reported that a diagonally generated, low-amplitude wave arrives prior to S_3. We also observe the arrival of a low-amplitude wave at 413 ns due to the generation of secondary waves at FS/Si interface (not shown). The normal displacements were measured at two different locations from two separate 600 nm Au film specimens each, and the displacement profiles were highly repeatable.

The substrate stress and the interface stress histories are evaluated from the displacement data by applying Eqs. (7)–(9). The evolution of the substrate shear stress, τ_{sub}, resulting from the incident wave S_3 is plotted in Fig. 11(c). The shear stress displays the characteristic linear ramp associated with a decompression shock, reaching a peak value of 0.49 GPa. The sharp change in substrate stress corresponds to the turnaround point in the fringe data. The interface stress histories normal to

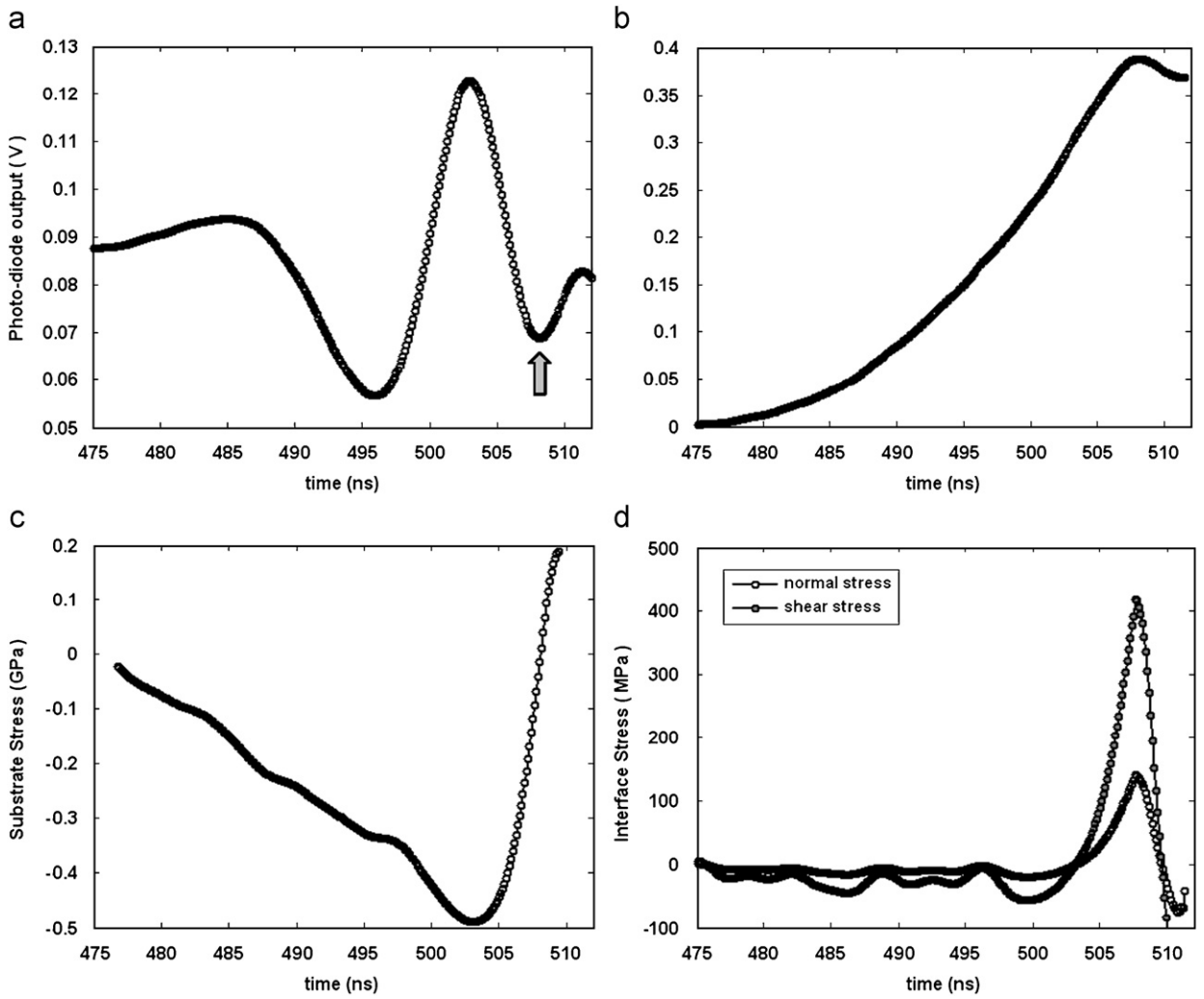

Fig. 11. Interferometric measurements obtained for a 600 nm Au film specimen ($\Gamma = 20\,\mathrm{mJ/mm^2}$, $p = 1.3\,\mathrm{mm}$). (a) Displacement fringes corresponding to the incident shear wave, S_3, (b) corresponding out-of-plane displacement history, (c) substrate shear stress, τ_{sub}, (d) normal (σ_{int}), and shear (τ_{int}) interface stresses.

Table 3
Effect of laser fluence on substrate and interface stresses for the 600 nm Au film specimen at fixed offset distanced, $p = 2.9\,\mathrm{mm}$

Laser fluence ($\mathrm{mJ/mm^2}$)	Shear substrate stress, τ_{sub} (GPa)	Out-of-plane interface stress, σ_{int} (MPa)	In-plane interface stress, τ_{int} (MPa)
27	0.21	71	212
33	0.25	115	345
53	0.44	146	439
57[a]	0.46	–	–
60[a]	0.53	–	–

[a] Significant film spallation occurred.

the substrate/film interface, σ_{int} and τ_{int}, are evaluated using Eqs. (8) and (9), respectively (Fig. 11(d)). The interface shear stress is relatively small until a sharp increase at 503 ns to a maximum value of 418 MPa. The corresponding maximum tensile stress, σ_{int}, is 141 MPa.

4.2.2. Mixed-mode interfacial strength

Interfacial failure is investigated at different offsets and for different Au film thicknesses. The effect of laser fluence is summarized in Table 3 for the 600 nm thick Au film for fixed offset distance ($p = 2.9\,\mathrm{mm}$). The maximum substrate shear

Table 4
Effect of offset distance on substrate and interface stresses in 1200 nm Au film specimen at fixed laser fluence, 67 mJ/mm^2

Offset distance p (mm)	Shear substrate stress, τ_{sub} (GPa)	Out-of-plane interface stress, σ_{int} (MPa)	In-plane interface stress, τ_{int} (MPa)
1.5[a]	0.53	135	406
3.7[a]	0.47	157	472
4.7[a]	0.40	132	395
7.6	0.32	68	203

[a] Significant film spallation occurred.

Table 5
Substrate and interface stresses just before failure initiation for different film thicknesses

Film thickness (nm)	Offset distance, p (mm)	Laser fluence (mJ/mm^2)	Substrate shear stress, τ_{sub} (GPa)	Out-of-plane interface stress, σ_{int} (MPa)	In-plane interface stress, τ_{int} (MPa)
300	2.75	31	0.25	141	423
	4.35	41	0.35	149	448
		44	0.36	142	427
600	1.50	41	0.40	146	439
	2.95	55	0.44	146	439
	4.45	75	0.35	142	425
1200	1.50	41	0.42	142	426
		55	0.49	133	400

stress increases with increasing laser fluence. Significant spallation occurs for incident laser fluences of 57 mJ/mm^2 and higher. The maximum shear and tensile interface stresses also increase monotonically with increasing laser fluence until spallation is detected. For the 600 nm thick film, the maximum shear and tensile interface stresses just prior to the interfacial failure are, $\tau_{int} = 439$ and $\sigma_{int} = 146$ MPa, respectively (at 53 mJ/mm^2 laser fluence). The influence of offset distance is summarized in Table 4 for the 1200 nm thick Au film at a constant fluence of 67 mJ/mm^2. The maximum substrate stress (in shear) decreases with increasing offset distance of incident YAG energy. The longer travel distance at larger offset leads to greater attenuation of the stress wave, causing lower substrate stress values. Interface stresses are reported in Table 4, even though significant film spallation was observed.

The stress values for all three film thickness just at or before interfacial failure initiation are presented in Table 5. In these experiments, the laser power is gradually increased until film damage is initiated. The maximum shear interface stress, τ_{int}, at initiation varies between 400 and 450 MPa for all the film thicknesses, with an average value of 426 ± 15 MPa. The error is one standard deviation from the average value for eight tests. The corresponding tensile interface stress value at initiation is 142 ± 5 MPa. Hence, the effective mixed-mode interfacial strength of the Au film on a passivated Si substrate is given by $\sigma_{eff} = \sqrt{(\sigma_{int}^2 + \tau_{int}^2)} = 449$ MPa. Only the experimental error is included in the reported error band. A central difference method was used to evaluate stresses from the displacement histories (Eqs. (7)–(9)), and the error associated with the numerical differentiation is estimated as ± 35 MPa.

4.2.3. Comparison of normal and mixed-mode interface strength

The intrinsic tensile strength between an Au film and a passivated Si substrate was determined via tensile laser spallation experiments. As described in Section 3.1, a tensile sample was fabricated by bonding a passivated Si substrate with a 300 nm thick Au film to a flat FS plate (Fig. 1). Laser fluence was gradually increased until tensile spallation was initiated. The out-of-plane displacement, substrate stress, and interface stress histories were evaluated from interferometric data as described by Wang et al. (2004). Tensile spallation was initiated at a laser fluence of 65 mJ/mm^2. The average maximum interface stress just before failure initiation was 245 ± 15 MPa, based on five experiments at each laser fluence from two different samples. When the Si_xN_y/Au interface is subjected to only tensile loading, the interfacial strength is approximately 100 MPa higher than the tensile interface stress at failure initiation measured under mixed-mode conditions (142 MPa). However, the effective mixed-mode strength is significantly larger, indicating more energy is required to fail the films under mixed-mode conditions. This result is consistent with the data reported by Wang et al. (2004) for a thin Al film on an isotropic substrate. We can also infer that the interfacial strength between an Au film and a passivated Si substrate in pure shear will be higher than 426 MPa.

5. Conclusions

The mixed-mode interfacial strength between an anisotropic substrate and an Au film was measured using a modified laser spallation technique. Mode mixity at the film interface was induced by directing a mode-converted refracted shear wave from the FS/Si interface oblique to the interface of interest. Selection of the specimen geometry and testing configuration was based on an analytical study of wave propagation across the FS/Si interface. Au films were deposited on a passivated Si substrate and subsequently bonded to a 45° FS prism. Due to the negative non-linearity of the FS prism, a laser-induced Gaussian stress pulse evolved into a decompression shock, which was successfully transmitted across the FS/Si interface for mode conversion. The wrinkling and tearing patterns of failed Au films were consistent with mixed-mode loading and differed significantly from the damage observed for the case of purely tensile loading. The interfacial stress history was inferred from interferometric measurements of free film surface displacement in combination with a detailed analytical wave propagation study. The shear component of the Si_xN_y/Au mixed-mode interfacial strength was 426 ± 15 MPa, and the normal stress component was142 ± 5 MPa. Comparatively lower transient tensile strength of the film interface (245 ± 15 MPa), obtained by performing separate experiments, indicated that the effective interfacial strength increased with mode mixity.

Appendix A

The characteristic wave equation for an anisotropic material is (Nayfeh, 1995)

$$C_{abcd}\frac{\partial^2 u_d}{\partial u_b \partial u_c} = \rho \frac{\partial^2 u_a}{\partial t^2}, \tag{A.1}$$

where C_{abcd} denotes the elements of the stiffness matrix and u_i is the displacement component in ith direction. The general solution to Eq. (A.1) is $u_d = Ap_d e^{\sqrt{-1}(kn_j x_j - \omega t)}$, where k, n_j, A, and p_d are the wave number, wave propagation direction, displacement amplitudes, and polarization vector, respectively. Substituting u_d into Eq. (A.1) and redefining terms yields the Christoffel equation

$$(A_{ad} - v_z^2 \delta_{ad}) p_d^{v_z} = 0, \tag{A.2}$$

where $A_{ad} = C_{abcd} n_c n_b / \rho$, $v_z = \omega/k$, and δ_{ad} is the Dirac delta function. Eq. (A.2) is an eigenvalue problem, which is solved for three wave velocities v_z, $z = 1, 2, 3$ with p^{v_z} representing the corresponding polarization vectors.

For a wave propagating in one of the $\langle 1\,0\,0 \rangle$ planes (x_1–x_2 plane) of a cubic material with an angle θ to the axis x_1, as shown in Fig. A1, the elements of the Christoffel equation are

$$\begin{aligned} A_{11} &= (C_{11}\cos^2\theta + C_{44}\sin^2\theta)/\rho, \\ A_{22} &= (C_{44}\cos^2\theta + C_{11}\sin^2\theta)/\rho, \\ A_{22} &= C_{44}/\rho, \\ A_{12} &= \{(C_{12} + C_{44})\cos\theta\,\sin\theta\}/\rho, \\ A_{13} &= A_{23} = 0, \end{aligned} \tag{A.3}$$

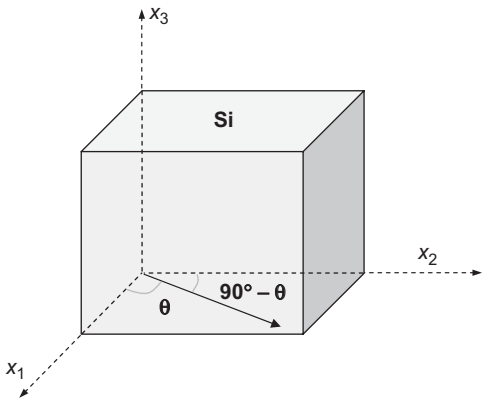

Fig. A1. Wave propagation in x_1–x_2 plane of a cubic material making an angle θ to the x_1 axis. Planes x_1–x_2, x_2–x_3, and x_3–x_1 are the planes of material symmetry.

where C_{11}, C_{44}, and C_{12} are cubic material constants. For a non-trivial solution of Eq. (2), the determinant $|A_{ad} - v_z^2\delta_{ad}|$ must vanish, yielding

$$v_1 = \sqrt{\frac{(C_{11}+C_{44}) + \sqrt{(C_{11}-C_{44})^2\cos^2 2\theta + (C_{12}+C_{44})^2\sin^2 2\theta}}{2\rho}},$$
$$v_2 = \sqrt{\frac{(C_{11}+C_{44}) - \sqrt{(C_{11}-C_{44})^2\cos^2 2\theta + (C_{12}+C_{44})^2\sin^2 2\theta}}{2\rho}},$$
$$v_3 = \sqrt{\frac{C_{44}}{\rho}}, \tag{A.4}$$

while the corresponding polarization vectors are

$$p^{v_1} = \left(1, \Delta - \sqrt{1+\Delta^2}, 0\right),$$
$$p^{v_2} = \left(1, \Delta + \sqrt{1+\Delta^2}, 0\right),$$
$$p^{v_3} = (0,0,1), \tag{A.5}$$

with $\Delta = (A_{22} - A_{11})/2A_{12}$. Clearly, v_3 corresponds to a pure shear wave with its polarization vector parallel to x_3. The other two waves, v_1 and v_2, are quasi-longitudinal and quasi-shear waves, respectively, with polarization vectors depending upon the direction of propagation.

The wave propagation across an isotropic/cubic bimaterial interface is shown schematically in Fig. 2. The displacements for the incident (L_1), reflected (L_2, S_2), and refracted (L_3, S_3, S_3') waves are assumed to have the form $u_d = Ap_d e^{\sqrt{-1}(kn_jx_j - \omega t)}$, where u_d are displacement components, p_d are polarization components, and A is the wave amplitude. Enforcing displacement continuity at the interface in x_1, x_2, and x_3 direction, we obtain

$$u_1^{L_1} + u_1^{L_2} + u_1^{S_2} = u_1^{L_3} + u_1^{S_3} \Rightarrow A_{L_1}p_1^{L_1} + A_{L_2}p_1^{L_2} + A_{S_2}p_1^{S_2} = A_{L_3}p_1^{L_3} + A_{S_3}p_1^{S_3},$$
$$u_2^{L_1} + u_2^{L_2} + u_2^{S_2} = u_2^{L_3} + u_2^{S_3} \Rightarrow A_{L_1}p_2^{L_1} + A_{L_2}p_2^{L_2} + A_{S_2}p_2^{S_2} = A_{L_3}p_2^{L_3} + A_{S_3}p_2^{S_3},$$
$$u_3^{S_3'} = 0 \Rightarrow A_{S_3'} = 0. \tag{A.6}$$

The stress components, σ_{22} and σ_{12}, for a wave propagating in a cubic symmetry plane x_1–x_2 are given as

$$\sigma_{22} = C_{11}\frac{\partial u_2}{\partial x_2} + C_{12}\frac{\partial u_1}{\partial x_1},$$
$$\sigma_{12} = C_{44}\left(\frac{\partial u_1}{\partial x_2} + \frac{\partial u_2}{\partial x_1}\right). \tag{A.7}$$

Substituting the displacement components for incident, reflected, and refracted waves in Eq. (A.7) and applying traction continuity in the x_1 and x_2 directions at the interface yields

$$\sigma_{12}^{L_1} + \sigma_{12}^{L_2} + \sigma_{12}^{S_2} = \sigma_{12}^{L_3} + \sigma_{12}^{S_3} \Rightarrow \sum_{j=L_1,L_2,S_2}\frac{A_j\{C_{44}(p_1n_2 + p_2n_1)\}_j}{v_j} = \sum_{j=L_3,S_3}\frac{A_j\{C_{44}(p_1n_2 + p_2n_1)\}_j}{v_j},$$
$$\sigma_{22}^{L_1} + \sigma_{22}^{L_2} + \sigma_{22}^{S_2} = \sigma_{22}^{L_3} + \sigma_{22}^{S_3} \Rightarrow \sum_{j=L_1,L_2,S_2}\frac{A_j(C_{11}p_2n_2 + C_{12}p_1n_1)_j}{v_j} = \sum_{j=L_3,S_3}\frac{A_j(C_{11}p_2n_2 + C_{12}p_1n_1)_j}{v_j}, \tag{A.8}$$

where the wave speeds, v_j, at a given angle, θ, are calculated from Eq. (A.4). The part of continuity equations and wave velocities for an isotropic material are evaluated assuming $C_{44} = (C_{11} - C_{12})/2$. Eqs. (A.6) and (A.8) are solved simultaneously to find amplitude ratios A_{L_2}/A_{L_1}, A_{S_2}/A_{L_1}, A_{L_3}/A_{L_1}, A_{S_3}/A_{L_1}, and $A_{S_3'}/A_{L_1}$.

Similarly, the amplitude ratios at the free film surface are computed by enforcing traction continuity tangential and normal to the surface. For example, the amplitude ratios of reflected waves, S_4 and L_4, are evaluated by solving the following equations:

$$\frac{A_{S_3}\{C_{44}(p_1n_2 + p_2n_1)\}_{S_3}}{v_{S_3}} + \frac{A_{S_4}\{C_{44}(p_1n_2 + p_2n_1)\}_{S_4}}{v_{S_4}} + \frac{A_{L_4}\{C_{44}(p_1n_2 + p_2n_1)\}_{L_4}}{v_{L_4}} = 0,$$
$$\frac{A_{S_3}(C_{11}p_2n_2 + C_{12}p_1n_1)_{S_3}}{v_{S_3}} + \frac{A_{S_4}(C_{11}p_2n_2 + C_{12}p_1n_1)_{S_4}}{v_{S_4}} + \frac{A_{L_4}(C_{11}p_2n_2 + C_{12}p_1n_1)_{L_4}}{v_{L_4}} = 0. \tag{A.9}$$

References

Cao, H.C., Evans, A.G., 1989. An experimental study of the fracture resistance of bimaterial interfaces. Mech. Mater. 7 (4), 295–304.
Charalambides, P.G., Cao, H.C., Lund, J., Evans, A.G., 1990. Development of a test method for measuring the mixed mode fracture resistance of bimaterial interfaces. Mech. Mater. 8 (4), 269–283.
Evans, A.G., Hutchinson, J.W., 1995. The thermomechanical integrity of thin films and multilayers. Acta Metall. Mater. 43 (7), 2507–2530.
Fukuhara, M., Sanpei, A., 1994. High temperature-elastic moduli and internal dilational and shear frictions of fused quartz. Jpn. J. Appl. Phys. 33 (5B), 2890–2893.
Gupta, V., Argon, A.S., Cornie, J.A., Parks, D.M., 1990. Measurement of interface strength by laser-pulse-induced spallation. Mater. Sci. Eng. A 126, 105–117.
Gupta, V., Kireev, V., Jun, T., Yoshida, H., Akahoshi, 2003. Glass-modified stress waves for adhesion measurement of ultra thin films for device applications. J. Mech. Phys. Solids 51 (8), 1395–1412.
Hall, J.J., 1967. Electronic effects in the elastic constants of n-type silicon. Phys. Rev. 161 (3), 756–761.
Hartfield, C.D., Ogawa, E.T., Park, Y.-J., Chiu, T.-C., Guo, H.L., 2004. Interface reliability assessment for copper/low-k products. IEEE Trans. Device Mater. Reliab. 4 (2), 129–141.
Hu, L., Wang, J., 2006. Pure-shear failure of thin films by laser-induced shear waves. Exp. Mech. 46 (5), 637–645.
Kandula, S.S.V., Hartfield, C.D., Geubelle, P.H., Sottos, N.R., 2008. Adhesion strength measurement of polymer dielectric interfaces using laser spallation technique. Thin Solid Films 516, 7627–7635.
Kim, K.-S., Kim, J., 1988. Elasto-plastic analysis of the peel test for thin film adhesion. J. Eng. Mater. Tech.—Trans. ASME 110 (3), 266–273.
Kriese, M.D., Gerberich, W.W., Moody, N.R., 1999a. Quantitative adhesion measures of multilayer films: Part I. Indentation mechanics. J. Mater. Res. 14 (7), 3007–3018.
Kriese, M.D., Gerberich, W.W., Moody, N.R., 1999b. Quantitative adhesion measures of multilayer films: Part II. Indentation of W/Cu, W/W, Cr/W. J. Mater. Res. 14 (7), 3019–3026.
Mittal, K.L., 1976. Adhesion measurement of thin films. Electrocomponent. Sci. Tech. 3, 21–42.
Nayfeh, A.H., 1995. Wave Propagation in Layered Anisotropic Media: With Applications to Composites. North-Holland Series in Applied Mathematics and Mechanics, Vol. 39. Elsevier, Amsterdam, New York.
Neighbours, J.R., Alers, G.A., 1958. Elastic constants of silver and gold. Phys. Rev. 3 (3), 707–712.
Thouless, M.D., 1989. Some mechanics for the adhesion of thin films. Thin Solid Films 181, 397–406.
Thouless, M.D., 1994. Fracture mechanics for thin-film adhesion. IBM J. Res. Dev. 38 (4), 367–377.
Vossen, J.L., 1978. Measurements of film-substrate bond strength by laser spallation. ASTM Special Technical Publication 640, 122–123.
Wang, J., Weaver, R.L., Sottos, N.R., 2002. A parametric study of laser induced thin film spallation. Exp. Mech. 42 (1), 74–83.
Wang, J., Weaver, R.L., Sottos, N.R., 2003. Laser induced decompression shock development in fused silica. J. Appl. Phys. 93 (12), 9529–9536.
Wang, J., Sottos, N.R., Weaver, R.L., 2004. Tensile and mixed-mode strength of a thin film-substrate interface under laser induced pulse loading. J. Mech. Phys. Solids 52 (5), 999–1022.
Wang, J.–S., Suo, Z., 1990. Experimental determination of interfacial toughness curves using Brazil-nut-sandwiches. Acta Metall. Mater. 38 (7), 1279–1290.
Yang, L.C., 1974. Stress waves generated in thin metallic films by a Q-switched ruby laser. J. Appl. Phys. 45 (6), 2602–2608.
Yu, H.H., He, M.Y., Hutchinson, J.W., 2001. Edge effects in thin film delamination. Acta Mater. 49 (1), 93–107.